PHYSICAL REVIEW FLUIDS **5**, 033701 (2020)

Bifurcations in the dynamics of a dipolar spheroid in a shear flow subjected to an external field

V. Kumaran
Department of Chemical Engineering, Indian Institute of Science, Bangalore 560 012, India

(Received 17 October 2019; accepted 21 January 2020; published 16 March 2020)

When a dipolar spheroid is subjected to a shear flow in the presence of an external field, there is a torque due to the dipole-field interaction which tends to align the spheroid in the direction of the field, and a torque due to the shear flow which tends to rotate the particle in closed "Jeffrey orbits." The presence of an external field is known to result in complex phase portraits containing a limit cycle along with multiple stationary points [Almog and Frankel, J. Fluid Mech. **289**, 243 (1995); Sobecki *et al.*, Phys. Rev. Fluids **3**, 084201 (2018)]. When the external field is in the flow plane, depending on the strength and orientation of the field, the phase portrait in orientation space could have two to six stationary nodes and/or a limit cycle. When the external field strength is low, there are two stationary points off the flow plane which are both stable/unstable and an unstable/stable limit cycle on the flow plane. When the external field strength is high, there is one stable node where the particle orientation is parallel to the field, and one unstable node where the particle orientation is anti-parallel to the field. As the external field strength is increased, the manner in which the phase portrait evolves depends on the external field orientation with respect to the flow direction and the particle shape factor. It is shown that complex phase portraits result from the relatively simple variations in the location of the stationary points in the orientation space as the parameter Σ is varied. Here Σ is the dimensionless ratio of the torques due to the external field and the shear flow. Depending on the aspect ratio of the particle, there are up to two saddle-node bifurcations, two subcritical bifurcations on the flow plane, and one reverse saddle-node merger of two stationary points off the flow plane. The limits of an ideal thin rod/disk are shown to be singular limits, where there are no stationary points off the flow plane even for a low external field, and the orientation of the particle changes discontinuously as the cross-stream component of the external field changes sign.

DOI: 10.1103/PhysRevFluids.5.033701

I. INTRODUCTION

Dipolar anisotropic particles in a suspension can be oriented in specific directions upon application of an external field, such as an electric or magnetic field. Particle orientation in a magnetic field has been used in microfluidic applications for separation of anisotropic particles due to lateral migration. An isolated particle in a uniform magnetic field does not experience a net force [1], though it does experience a torque. Lateral migration requires nonuniform magnetic fields or particle interactions with other particles or with a wall. Lateral migration due to wall interactions has been observed in experiments [2,3], and there have been some theoretical studies on the effect of far-field interactions on lateral migration [4,5].

Dipolar particles in electric fields have also been studied, though they are more limited in applications because the suspending medium is often polarizable and could contain mobile charges which screen the electric field near electrodes. There is also the possibility of dielectric breakdown for large electric fields. There have been early studies [6–8] on the effect of electric fields on the orientation of dipolar particles subjected to a shear flow and to Brownian forces, though these do not appear to have been as useful as electrokinetic flows driven by ion motion in microfluidic applications.

In applications such as magnetorheology, a suspension of ferromagnetic particles could be jammed due to the application of a magnetic field in the cross-stream direction. The jamming is attributed to the alignment of the anisotropic rodlike particles in the direction perpendicular to the flow. While the mechanism of jamming of a suspension of ferromagnetic particles is a subject of active research, the immense potential is being realized in applications such as brakes, dampers, and shock absorbers [9]. The critical parameter is the Mason number [10], which is the ratio of the hydrodynamic torque due to the shear flow and the torque due to the magnetic field. The jamming "transition" takes place at a critical Mason number where the aligning effect of the magnetic field exceeds the tendency of the mean shear to rotate the particles. The effect of the magnetic field is usually expressed as a "yield" stress [11], which is the minimum shear stress required to deform the material. Though the rheology of magnetorheological fluids have been widely studied using phenomenological models [12–14] and microscopic models [15,16], there have been relatively fewer efforts to relate the particle orientational transitions to jamming in magnetorheological fluids [17]. It should be noted that jamming is likely a collective effect which occurs only when the suspension is sufficiently concentrated, and interparticle interactions are likely to be very important for jamming. However, orientational transitions happen even in dilute systems, due to bifurcations in single-particle dynamics when subjected to shear and an external field, and these could have a significant effect on the rheology. Moreover, it is important to have an accurate understanding of single-particle dynamics before progressing to examine particle interactions.

In the absence of a magnetic field, anisotropic spheroids rotate in closed orbits called Jeffrey orbits [18,19]. When a magnetic field is applied, the particles tend to align in the direction of the magnetic field. The interplay between the magnetic torque and the hydrodynamic torque could give rise to complex behavior depending on their relative strengths. The dynamics of a spheroid in an external field in a shear flow was studied by Puyesky and Frankel [20] for a spherical particle and Almog and Frankel [21] for a spheroid in three dimensions, and more recently by Sobecki *et al.* [22] in two dimensions in the plane of shear. Almog and Frankel [21] studied the evolution of the azimuthal and meridional angles of the orientation vector of the spheroid as a function of the intensity and orientation of the external field. When the field is perpendicular to the plane of the flow, the particles align with the orientation vector perpendicular to the plane of the flow and rotate with an angular velocity equal to the fluid rotation rate. Interesting behavior is observed when the external field is in the plane of shear. When the field amplitude is very large, there are two stationary points, a stable fixed point where the orientation vector is parallel to the external field, and an unstable fixed point where the orientation vector is opposite in direction to the external field. When the orientation of the external field is not parallel to the flow plane, it is found that there are two fixed points solutions for the orientation vector, but the relaxation time for the convergence of the orientation towards these fixed points increases inversely proportional to the field strength. The most interesting behavior was observed when the direction of the external field is in the flow plane.

For a spherical dipolar particle, Almog and Frankel [21] studied the case where the orientation of the external field is in the flow plane. It was shown that there is a critical value of the field below which there are stable orbits, and above which there is one stable and one unstable fixed point. The critical field strength and the orientation for the stable and unstable fixed points can be determined analytically for a spherical dipolar particle. For prolate spheroids, Almog and Frankel [21] showed that there are fixed points off the flow plane when the external field intensity is below a critical value, but these are stable/unstable spiral points when the external field is not oriented in either the flow or cross-stream directions. When the external field intensity is increased, there is a series of possibilities including two fixed points on the flow plane and two off the flow plane, as well as four fixed points on the flow plane and two off the flow plane. These invariably occur through a series of subcritical and saddle-node bifurcations depending on the magnitude and orientation of the external field. Sobecki *et al.* [22] have solved for the evolution of the meridional angle of the orientation vector in the flow plane and have shown that there are certain values of the field intensity and orientation when there are four fixed points with orientation in the flow plane. In the two-dimensional parameter space comprising the external field strength and orientation, regions containing zero, two, and four solutions have been identified. Almog and Frankel [21] have studied the solutions for the orientation vector off the flow plane and have found that these could coexist with solutions where the orientation is on the flow plane.

There are two objectives of the present analysis. The first is to identify the nature of the bifurcations that lead to different kinds of phase behavior for a dipolar prolate spheroid. A detailed analysis of the trajectories of the azimuthal and meridional angles of the fixed points in phase space shows the classification of and the connection between different fixed points. In addition, bifurcation diagrams showing the appearance and evolution of the fixed points with external field strength are shown; these reveal the sequence of bifurcations which lead to different topologies of the phase portraits.

The second objective is to consider the case of a thin rod, which is shown to be a singular limit of the general prolate spheroid. When the external field is not in the flow plane, there are two stable fixed points for the rod orientation even for small external field strength. Interestingly, the particle orientation angle shows a large variation when the component of the external field orientation vector in the cross-stream direction transitions from a positive to a negative value. When the external field is parallel to the flow plane, the domains in parameter space where there are four fixed points are identified analytically, and the nature of the fixed points is examined.

After briefly discussing previous relevant results for the Jeffrey orbits for low external field, the orientation for high external field, and the dynamics of a spherical particle, the dynamics of a thin rod is analyzed in Sec. III. The phase plots and the phase-space trajectories for the orientation vector of a prolate spheroid is considered in Sec. IV. Bifurcation diagrams showing the sequence of bifurcations are used to explain the reasons for the different numbers and types of fixed points in the phase plots.

II. EVOLUTION EQUATIONS

The configuration consists of a spheroid with orientation unit vector $\boldsymbol{p}$ of the axis of rotation and dipole moment $\boldsymbol{m}$ along the orientation vector placed in a shear flow with strain rate $\dot{\gamma}$ subjected to an external field $\boldsymbol{H}$. The evolution equations for the particle orientation are defined in a reference frame, (X, Y, Z), where the flow velocity is in the X direction, the velocity gradient in the Y direction, and the Z direction is perpendicular to the plane of the flow, as shown in Fig. 1. The Euler angles ϕ, θ are the angles of sequential rotation of the (X, Y, Z) axes, first about the Z axis and then about the X axis, so that the Z axis and orientation vector $\boldsymbol{p}$ are aligned. The azimuthal angle θ, which varies between 0 and π, is the angle made by the orientation vector with the Z axis. The meridional angle ϕ is the angle made by the projection of the orientation vector on the X-Y plane with the $-Y$ axis. This is different from the usual convention where the angle from the X axis is ϕ; however, this notation is used here since it is the result of the sequence of rotations prescribed by Goldstein [23], which is standard in the field. The components of the orientation vector in the three coordinate directions are

$$\boldsymbol{p} = \sin(\theta)\sin(\phi)\hat{\boldsymbol{X}} - \sin(\theta)\cos(\phi)\hat{\boldsymbol{Y}} + \cos(\theta)\hat{\boldsymbol{Z}}, \tag{1}$$

where $\hat{\boldsymbol{X}}$, $\hat{\boldsymbol{Y}}$, and $\hat{\boldsymbol{Z}}$ are the unit vectors in the three coordinate directions. The Euler angles (ξ, η) of the unit vector in the direction of the external field, $\hat{\boldsymbol{H}}$, are defined analogous to the angles (θ, ϕ) of the particle orientation vector.

The evolution equations for the Euler angles are derived from the torque balance condition that the sum of the hydrodynamic and magnetic torques is zero in the absence of fluid inertia. The magnetic torque on the particle in the external field is

$$\begin{aligned} T_X^m &= mH[\cos(\theta)\sin(\xi)\cos(\eta) - \cos(\xi)\sin(\theta)\cos(\phi)], \\ T_Y^m &= mH[\cos(\theta)\sin(\xi)\sin(\eta) - \cos(\xi)\sin(\theta)\sin(\phi)], \\ T_Z^m &= mH\sin(\xi)\sin(\theta)\sin(\eta-\phi), \end{aligned} \tag{2}$$

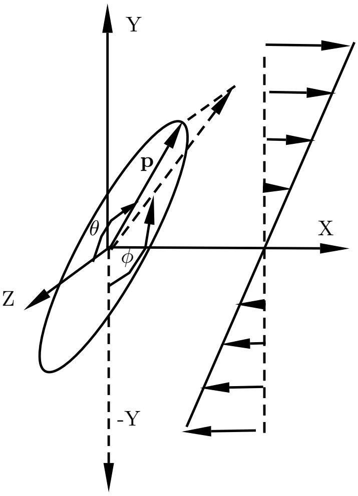

FIG. 1. The coordinate system for analyzing the orientation of a spheroid in a linear shear flow and the Euler angles θ and ϕ in this configuration.

where $m = |\boldsymbol{m}|$ and $H = |\boldsymbol{H}|$. The hydrodynamic torque has been derived earlier in Refs. [18] and [19], and the derivation is not repeated here. From the torque balance conditions, the evolution equations for the Euler angles θ and ϕ [21] are

$$\frac{d\theta}{dt^*} = -\frac{B}{4}\sin(2\theta)\sin(2\phi) + \Sigma[\sin(\xi)\cos(\theta)\cos(\phi-\eta) - \cos(\xi)\sin(\theta)], \tag{3}$$

$$\frac{d\phi}{dt^*} = -\frac{1}{2} - \frac{B}{2}\cos(2\phi) - \Sigma[\sin(\xi)\csc(\theta)\sin(\phi-\eta)], \tag{4}$$

where the scaled time is defined as $t^* = \dot{\gamma}t$, the product of the strain rate and time, and the dimensionless parameter Σ is defined as

$$\Sigma = \frac{mH(\alpha_x^* + r^2\alpha_z^*)}{16\pi\mu R^3(1+r^2)\dot{\gamma}}, \tag{5}$$

where r is the ratio of the length along the axis of rotation and the maximum diameter perpendicular to the axis of rotation, the shape factor $B = (r^2-1)/(r^2+1)$, R is the maximum radius perpendicular to the axis of rotation, μ is the viscosity, and the parameters α_x^* and α_z^* are scaled elliptic integrals,

$$\alpha_i^* = R\int_0^\infty \frac{d\lambda}{(R_i^2+\lambda)\sqrt{(R_x^2+\lambda)(R_y^2+\lambda)(R_z^2+\lambda)}}, \tag{6}$$

where $R_x = R_y = R$ is the radius perpendicular to the axis of rotation, and $R_z = rR$ is one half of the length along the axis of rotation.

Steady solutions of Eqs. (3) and (4), (θ_s, ϕ_s), are obtained by setting the right sides of the equations equal to zero. The stability of the steady solutions are determined by examining the response to small perturbations, (θ', ϕ'), imposed on the steady solutions (θ_s, ϕ_s), and linearizing the equations in perturbations,

$$\begin{pmatrix} \frac{d\theta'}{dt^*} \\ \frac{d\phi'}{dt^*} \end{pmatrix} = \mathbf{L}\begin{pmatrix} \theta' \\ \phi' \end{pmatrix}, \tag{7}$$

where the linear stability matrix $\mathbf{L}$ is

$$\mathbf{L} = \begin{pmatrix} \begin{array}{l} -\frac{B}{2}\cos(2\theta_s)\sin(2\phi_s) \\ \quad -\Sigma[\sin(\xi)\sin(\theta_s)\cos(\phi_s-\eta) \\ \quad +\cos(\xi)\cos(\theta_s)] \end{array} & \begin{array}{l} -\frac{B}{2}\sin(2\theta_s)\cos(2\phi_s) \\ \quad -\Sigma\sin(\xi)\cos(\theta_s)\sin(\phi_s-\eta) \end{array} \\ \Sigma\sin(\xi)\sin(\phi_s-\eta)\cot(\theta_s)\csc(\theta_s) & B\sin(2\phi_s)-\Sigma\sin(\xi)\csc(\theta_s)\cos(\phi_s-\eta) \end{pmatrix}. \tag{8}$$

The eigenvalues of the $\mathbf{L}$ matrix, which determine the stability of the solution, are denoted λ_1 and λ_2 if they are real, and $\lambda_R \pm \imath\lambda_I$ if they are complex. For future reference, when the external field and the particle orientation are along the flow plane, $\xi = \pi/2$ and $\theta_s = \pi/2$, the matrix $\mathbf{L}$ is

$$\mathbf{L} = \begin{pmatrix} -\Sigma\cos(\phi_s-\eta)+(B/2)\sin(2\phi_s) & 0 \\ 0 & -\Sigma\cos(\phi_s-\eta)+B\sin(2\phi_s) \end{pmatrix}. \tag{9}$$

In this case, the two eigenvalues are $\lambda_\theta = -\Sigma\cos(\phi_s-\eta)+(B/2)\sin(2\phi_s)$ and $\lambda_\phi = -\Sigma\cos(\phi_s-\eta)+B\sin(2\phi_s)$.

A. Symmetries

In Eqs. (3) and (4) the angles η and ϕ vary in the range $-\pi$ to π, and θ and ξ vary in the range 0 to π. The following symmetry transformations of Eqs. (3) and (4) are used to relate the phase portraits for different parameter values:

(1) Equations (3) and (4) are invariant under the transformation $\eta \to \eta \pm \pi$ and $\phi \to \phi \pm \pi$.

(2) Equation (3) and (4) are invariant under the transformation $\eta \to -\eta$, $\phi \to \pi - \phi$ and $\theta \to \pi - \theta$.

(3) Under the transformation $\xi \to \pi - \xi$ and $\theta \to \pi - \theta$, the rates of evolution of the angles in Eqs. (3) and (4) transform as $(d\theta/dt^*) \to -(d\theta/dt^*)$ and $(d\phi/dt^*) \to (d\phi/dt^*)$.

(4) For $\xi = \pi/2$, when the external field is in the X-Y plane, under the transformation $\eta \to \pi - \eta$ and $\phi \to -\phi$, the rates of evolution of the angles in Eqs. (3) and (4) transform as $(d\theta/dt^*) \to -(d\theta/dt^*)$ and $(d\phi/dt^*) \to (d\phi/dt^*)$.

(5) Equations (3) and (4) are invariant under the transformation $B \to -B$, $\phi \to (\phi + \pi/2)$ and $\eta \to (\eta + \pi/2)$.

The above symmetry transformations, which were first discussed in Ref. [21], significantly reduce the parameter space for analysis. It is sufficient to consider prolate spheroids with $B > 0$, because symmetry 5 above can be used to determine the equivalent results for an oblate spheroid with $B < 0$. In addition, it is sufficient to consider the parameter regime $0 \leqslant \xi \leqslant \pi/2$ due to symmetry 3, $0 \leqslant \theta \leqslant \pi/2$ due to symmetry 2, and $0 \leqslant \eta \leqslant \pi$ due to symmetry 1.

B. No external field

The Jeffrey orbits are recovered in the absence of a external field, i.e., for $\Sigma = 0$. The equation for $(d\phi/dt^*)$ is independent of θ, and the angle ϕ varies periodically in time,

$$\tan(\phi) = -\sqrt{\frac{1+B}{1-B}}\tan(\omega_J t^*), \tag{10}$$

where the "Jeffrey frequency" ω_J is

$$\omega_J = \frac{\sqrt{1-B^2}}{2}. \tag{11}$$

The angle θ is related to ϕ by the equation

$$\tan(\theta) = C\left[\left(\frac{1+B}{1-B}\right)\cos(\phi)^2 + \sin(\phi)^2\right]^{-1/2}, \tag{12}$$

where C is a constant which depends on the initial condition.

C. High external field

In the limit $\Sigma \gg 1$, the particles are expected to be nearly aligned with the external field, that is, $\theta = \xi$ and $\phi = \eta$. A regular perturbation expansion can be used in the small parameter Σ^{-1} to obtain the difference between the particle and external field alignment:

$$\theta_s - \xi = -\Sigma^{-1} B \sin(\xi)\cos(\xi)\sin(\eta)\cos(\eta), \tag{13}$$

$$\phi_s - \eta = -\tfrac{1}{2}\Sigma^{-1}[B\cos(2\eta) + 1]. \tag{14}$$

The external torque on the particle in the fixed reference frame is

$$T_X^m = -\tfrac{1}{2} m H \Sigma^{-1}(1 - B)\sin(\xi)\cos(\xi)\sin(\eta), \tag{15}$$

$$T_Y^m = \tfrac{1}{2} m H \Sigma^{-1}(1 + B)\sin(\xi)\cos(\xi)\cos(\eta), \tag{16}$$

$$T_Z^m = \tfrac{1}{2} m H \Sigma^{-1}\sin(\xi)^2[1 + B\cos(2\eta)]. \tag{17}$$

D. Spherical particle

The shape factor B is zero for a spherical particle, and the simplified evolution Eqs. (3) and (4) depend only on the angles ξ, θ, and $(\phi - \eta)$. The steady solutions for Eqs. (3) and (4) are

$$\begin{aligned} \sin(\theta_s) &= \sqrt{\frac{1+4\Sigma^2}{2} - \frac{\sqrt{(1+4\Sigma^2)^2 - 16\Sigma^2\sin(\xi)^2}}{2}}, \\ \sin(\phi_s - \eta) &= -\frac{\sin(\theta_s)}{2\Sigma\sin(\xi)}, \\ \cos(\phi_s - \eta) &= \frac{\tan(\theta_s)}{\tan(\xi)}. \end{aligned} \tag{18}$$

There are two fixed-point solutions in Eq. (18) with $\cos(\theta_s) = \pm\sqrt{1 - \sin(\theta_s)^2}$; $\sin(\phi_s - \eta)$ is the same for the two solutions, while $\cos(\phi_s - \eta)$ is of opposite sign. From Eq. (8), it is inferred that the elements of the linear stability matrix for the two solutions are equal in magnitude and opposite in sign, and therefore the eigenvalues have real parts that are of equal magnitude and opposite sign. This indicates that either both solutions are neutral/saddle fixed points or one solution is stable while the other is unstable. When the external field is not in the flow plane, one of the fixed points is a stable spiral node, while the other is an unstable spiral node.

When the external field is aligned in the flow plane, $\xi = \pi/2$, the evolution of the fixed points is not continuous, but there is a bifurcation at a critical external field strength of $\Sigma = 0.5$. Though this has been reported before, the phase plots and sample trajectories in the θ_s,ϕ_s plane are shown in Fig. 2 for comparison with results for a spheroid. The left and right halves of these phase plots are a mirror images about the vertical line $\theta = \pi/2$, and therefore the phase plots are shown in the left half of the figure and sample trajectories are shown in the right half.

When Σ is less than 0.5 there are two center nodes at $\phi_s - \eta = -\pi/2$ and $\sin(\theta_s) = 2\Sigma$ which are equidistant from the $\theta = \pi/2$ line, as shown in Fig. 2(a). For the center nodes, the linear stability matrix $\mathbf{L}$ [Eq. (8)] has two imaginary eigenvalues, $\pm\imath\Sigma\cot(\theta_s) = (\pm\imath\sqrt{1-4\Sigma^2}/2)$. It may be recalled that for the Jeffrey orbits in the absence of a external field, the frequency of the particle rotation has a fixed frequency independent of the initial orientation of the particles. In the presence of a external field, it is found that the variation of the frequency with the initial angle of orientation is $O(10^{-3})$ times smaller than the actual frequency, and so it is numerically accurate to consider the frequency as independent of the initial orientation. The frequency for the periodical orbits around the center node is numerically close to $\omega = (\sqrt{1-4\Sigma^2}/2)$.

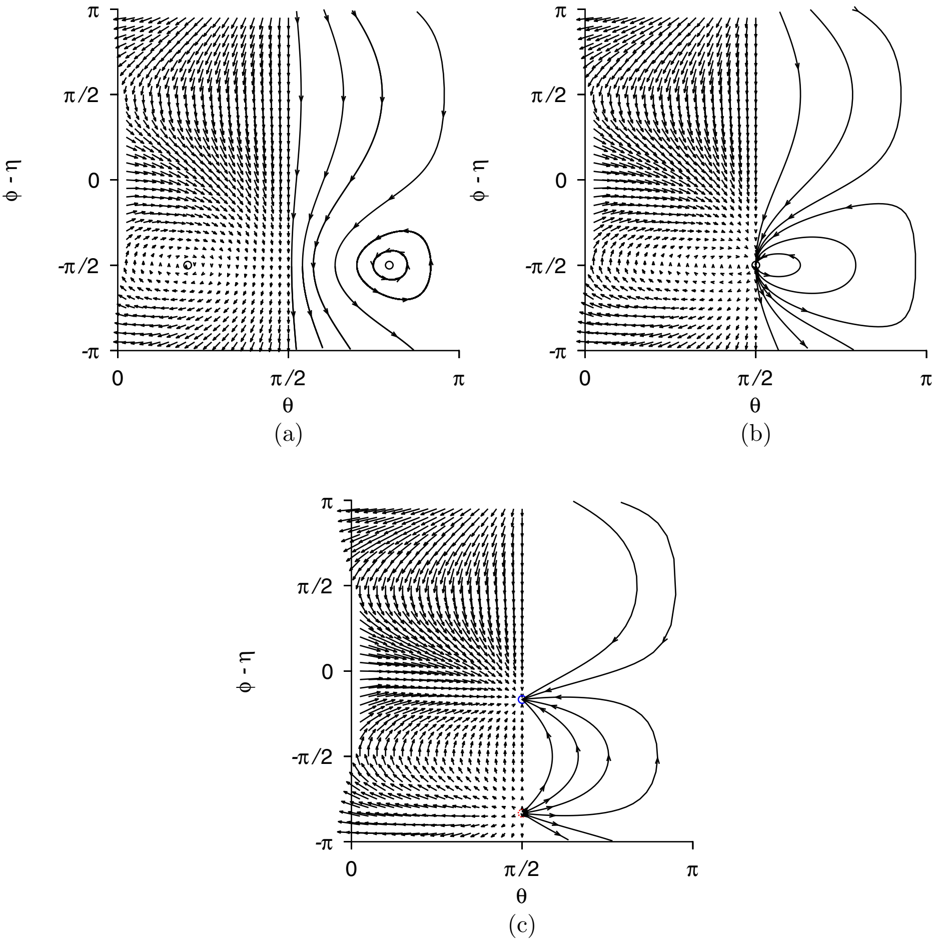

(a)

(b)

(c)

FIG. 2. The phase portrait in the θ vs ϕ-η plane (left half) and sample trajectories (right half) for a spherical particle ($B = 0$) with $\xi = \pi/2$ and $\Sigma = 0.3$ (a), $\Sigma = 0.5$ (b), and $\Sigma = 1.0$ (c). In panels (a) and (b), the black circles are neutrally stable nodes. In panel (c), the solid blue circle is the stable node, and the dashed red circle is the unstable node.

When Σ is increased to 0.5, the two center nodes approach and merge at $\phi_s - \eta = -\pi/2$ and $\theta_s = \pi/2$, as shown in Fig. 2(b). When Σ is increased above 0.5, a stable and unstable node emerge at $\theta_s = \pi/2$ and for two different values of ϕ_s which satisfy the relation $\sin(\phi_s - \eta) = -(2\Sigma)^{-1}$. The linear stability matrix $\mathbf{L}$ [Eq. 11] has repeated eigenvalues $\lambda_1 = \lambda_2 = -\Sigma\cos(\phi_s) = \pm(\sqrt{4\Sigma^2 - 1}/2)$; the stationary point with $\phi_s > -\pi/2$ is a stable node while that with $\phi_s < -\pi/2$ is an unstable node.

III. THIN ROD

A. Small external field

When there is no external field, the trajectories of the orientation vector are great circles on the unit sphere which intersect on the X axis, $\phi = \pm\pi/2$. The Jeffrey frequency [Eq. (11)] decreases to 0 proportional to $(1 - B)^{1/2}$. When a small external field is applied, the external field stabilises the orientation vector near the X axis, at $\theta_s = \pi/2$ and at $\phi_s = \pm\pi/2$ depending on whether the

Y component of the external field is positive or negative. In the limit $\Sigma \ll 1$, steady solutions are obtained using an expansion in the small parameter $\Sigma^{1/2}$:

$$\theta_s = \frac{\pi}{2} - \frac{\sqrt{\Sigma}\cos(\xi)}{\sqrt{\sin(\xi)|\cos(\eta)|}}, \tag{19}$$

$$\phi_s = \pm\frac{\pi}{2} + \sqrt{\Sigma\sin(\xi)|\cos(\eta)|}. \tag{20}$$

In Eq. (20) the positive sign is applicable on the right side for $\cos(\eta) < 0$, and the negative sign is applicable for $\cos(\eta) > 0$. The mathematical reason for discontinuous change in orientation is the change in sign of the eigenvalues of the stability matrix $\mathbf{L}$ [Eq. (9)] at the two nodes at $\phi_s = \pm\pi/2$. The physical reason for these choices is as follows. The fluid vorticity rotates the particle in the clockwise direction in the X-Y plane, and stable solutions are obtained when the direction of the external torque is opposite to that of the hydrodynamic torque. If $\cos(\eta)$ is negative and the cross-stream component of the external field is in the $+Y$ direction, there is a balance of torques when the particle orientation is in the first quadrant in the X-Y plane and ϕ_s is close to $(\pi/2)$. If $\cos(\eta)$ is positive and the cross-stream component of the external field is in the $-Y$ direction, there is torque balance when the particle orientation is in the third quadrant of the X-Y plane and ϕ_s is close to $-(\pi/2)$. The components of the external torque on the particle for the stable fixed point are

$$T_X^m = \tfrac{1}{6} mH\Sigma^{3/2}\cos(\xi)\cos(\eta)\sqrt{\sin(\xi)|\cos(\eta)|}[2\cos(\xi)\cot(\xi)\sec(\eta)^2 + \sin(\xi)], \tag{21}$$

$$T_Y^m = \pm mH[\cos(\xi) + \sqrt{\Sigma|\cos(\eta)|\sin(\xi)}\cos(\xi)\tan(\eta)], \tag{22}$$

$$T_Z^m = \pm mH[\sin(\xi)\cos(\eta) + \sqrt{\Sigma|\cos(\eta)|\sin(\xi)}\sin(\eta)\sin(\xi)]. \tag{23}$$

In Eqs. (22) and (23) the positive/negative sign is applicable when $\cos(\eta)$ is positive/negative. Equation (22) shows that there is a discontinuity in the torques T_Y^m when the Y component of the external field changes sign, though the other two components pass through zero.

From Eq. (21) the torque T_X^m is proportional to $\Sigma^{3/2}$ for $\Sigma \ll 1$, because the rod is aligned close to the X direction. In the limit $\Sigma \gg 1$, Eq. (15) shows that T_X^m is identically zero for a thin rod ($B = 1$). This suggests that T_X^m is numerically small over the entire range of Σ; in numerical simulations, it is found that the the torque T_X^m is numerically smaller than the other components of the torque. Equation (16) shows that the torque T_Y^m is a continuous function of η for $\Sigma \gg 1$, whereas Eq. (22) indicates that the torque changes discontinuously at $\cos(\eta) = 0$ for $\Sigma \ll 1$.

The solutions (19) and (20) can be generalized for an oblique magnetic field, by carrying out an asymptotic analysis of the evolution Eqs. (3) and (4) for $\Sigma \ll 1$ and $(1 - B) \sim \Sigma$. In this limit, the generalization of the solutions (19) and (20) are

$$\phi_s \mp \frac{\pi}{2} = \sqrt{\Sigma\left[\sin(\xi)|\cos(\eta)| - \frac{(1-B)}{2\Sigma}\right]}, \tag{24}$$

$$\theta_s = \frac{\pi}{2} - \frac{\Sigma\cos(\xi)}{\phi_s \mp \pi/2}, \tag{25}$$

where the negative/positive sign is used for $\cos(\eta) \lessgtr 0$. Equation (24) shows that the above steady solutions exist only for $\Sigma > \{(1 - B)/2[\sin(\xi)|\cos(\eta)|]\}$.

The solutions in Eqs. (24) and (25) are clearly not applicable for $\cos(\eta) \to 0$. In this case, it is necessary to carry out an asymptotic expansion in the limit $(1 - B) \ll 1$ and $(\pi/2 - \eta) \ll 1$. Asymptotic matching of the terms on the right in the evolution Eqs. (3) and (4) indicates that the appropriate scalings are $(\pi/2 - \eta) = \sqrt{1-B}\eta'$, $\phi = -\pi/2 - \sqrt{1-B}\phi'$ and $\Sigma = \sqrt{1-B}\Sigma'$. The solutions for the angles θ and ϕ' are then obtained using an expansion of Eqs. (3) and (4) in the parameter $\sqrt{1-B}$. The following implicit equation provides the solution for θ:

$$\cos(\theta)^2\sin(\theta) + 2\Sigma'^2\cos(\xi)\sin(\theta + \xi) - 2\Sigma'\eta'\cos(\theta)^2\sin(\xi) = 0, \tag{26}$$

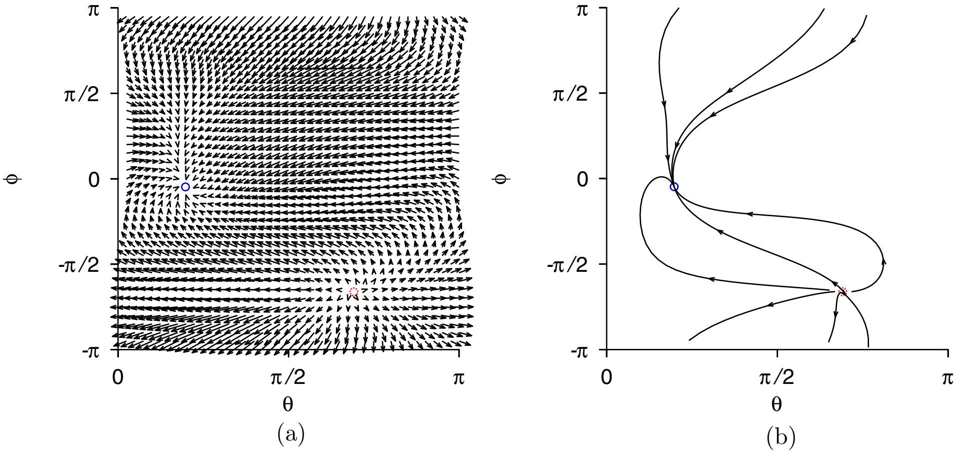

FIG. 3. The phase portrait in the θ vs ϕ plane (a) and sample trajectories (b) for a thin rod ($B = 1$) with $\xi = \pi/4$, $\eta = \pi/4$, and $\Sigma = 1.0$. The solid blue circle is the stable node, and the dashed red circle is the unstable node.

and the solution for ϕ' is

$$\phi' = -\Sigma'[\cos(\xi)\sec(\theta) + \sin(\xi)\csc(\theta)]. \tag{27}$$

It can also be shown that steady solutions for Eq. (27) exist only for

$$\Sigma' > \frac{\eta' \cos(\theta_0)^4 \tan(\xi)}{\sin(\xi)\cos(\theta_0)[\cos(\theta_0)^2 - \sin(\theta_0)^2] - 2\cos(\xi)\sin(\theta_0)^3}, \tag{28}$$

where θ_0 is a solution of the equation

$$\{2\cos(\xi)\sin(\theta_0)^3 + \sin(\xi)\cos(\theta_0)[\sin(\theta_0)^2 - \cos(\theta_0)^2]\}^2 + 2\eta'^2\cos(\theta_0)^4\sin(\xi)^2[1 + \sin(\theta_0)^2 + \sin(\theta_0)\cos(\theta_0)\tan(\xi)] = 0. \tag{29}$$

B. Oblique external field

The steady solutions, which are obtained numerically, contain one stable and one unstable fixed point. An example of the phase plots and sample trajectories for the specific case $\Sigma = 1$, $\xi = \pi/4$, and $\eta = \pi/4$ are shown in Fig. 3. The presence of one stable and one unstable fixed point is clearly visible here, and all trajectories converge to the stable fixed point in the long-time limit.

The angles (θ_s, ϕ_s) for the stable fixed point are shown as a function of Σ for $\xi = \pi/4$ and for different values of η in Fig. 4(a), and the components of the torque exerted on the particle are shown in Fig. 4(b). The steady solutions for the angles and the torque are consistent with the asymptotic solutions in Eqs. (13)–(17) for high Σ and with Eqs. (19)–(23) for low Σ.

An unusual feature observed in Fig. 4 is the large change in the orientation for small Σ when the angle of inclination η is slightly smaller than $\pi/2$. This is related to the switch in the sign in Eqs. (20), (22), and (23) when $\cos(\eta)$ passes through 0. When η is slightly less than $\pi/2$, Eq. (20) predicts that ϕ_s is $-\pi/2$ for small Σ, whereas Eq. (14) predicts that $\phi_s = \eta$ for large Σ. There is a sharp increase in ϕ_s at an intermediate value of Σ from $-\pi/2$ to a value close to $\pi/2$. This is accompanied by a large variation in θ_s in Fig. 4(a).

For the special case $\eta = \pm\pi/2$ [$\cos(\eta) = 0$], the external field is in the X-Z plane. For an infinitesimal thin rod, there is no hydrodynamic torque if the particle is also aligned in the X-Z plane, and therefore the torque balance results in the trivial solution $\theta_s = \xi$ and $\phi_s = \eta$. For η near $\pm\pi/2$, the effect of the hydrodynamic and external torques are comparable for $|\pm\pi/2 - \eta| \sim \Sigma^{1/2}$.

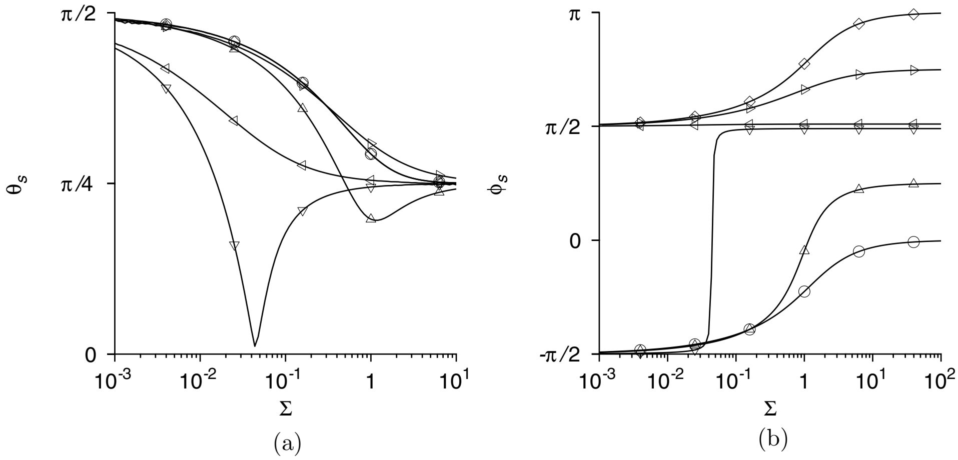

(a) (b)

FIG. 4. The values of θ_s (a) and ϕ_s (b) as a function of Σ for a thin rod ($B = 1$) with $\xi = \pi/4$ and $\eta = 0$ (○), $\eta = \pi/4$ (△), $\eta = 49\pi/100$ (∇), $\eta = 51\pi/100$ (◁), $\eta = 3\pi/4$ (▷), $\eta = \pi$ (⋄).

The external torque on the particle is shown as a function of Σ in Fig. 5. Since T_X^m is numerically small, it is not shown in Fig. 5. The torques in the Y and Z directions are consistent with the asymptotic results in Eqs. (22) and (23). The discontinuity in the torque T_Y^m at $\eta = (\pi/2)$ and $\Sigma \ll 1$ is evident in Fig. 5(a). This is due to the change in sign of the solution for ϕ_s in Eq. (20), resulting in the change in sign in Eq. (22) for the torque. Equation (23) predicts that the torque in the Z direction is continuous as η passes through $(\pi/2)$; this is consistent with the result in Fig. 5(b). There is a large variation in the torque T_Y^m for $\eta = (49\pi/100)$ in the range $3 \times 10^{-2} \lesssim \Sigma \lesssim 8 \times 10^{-2}$ in Fig. 5; this reflects the sharp variation in the angles θ_s and ϕ_s in the same parameter ranges in Fig. 4.

C. Parallel external field

When the external field is in the X-Y plane ($\xi = \pi/2$), it is easily shown that for the steady solutions, the orientation of the particle is necessarily in the X-Y plane, and $\theta_s = \pi/2$. The right

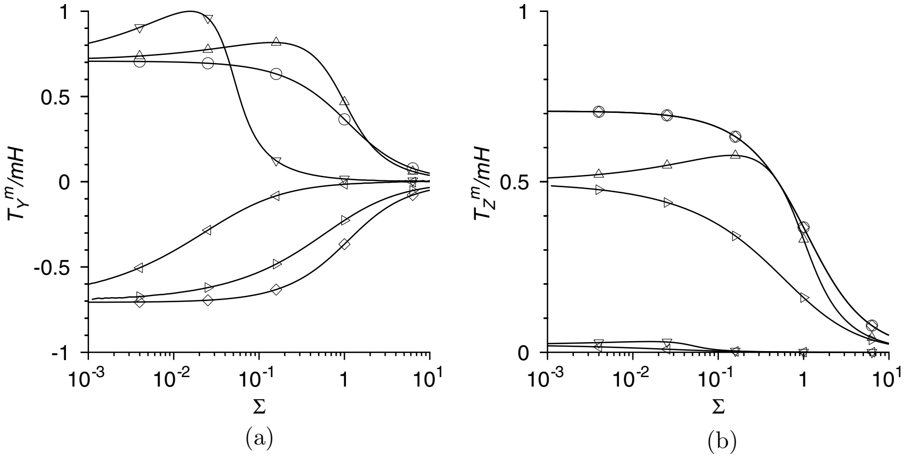

(a) (b)

FIG. 5. The torques T_Y^m (a) and T_Z^m (b), scaled by (mH), as a function of Σ for a thin rod ($B = 1$) with $\xi = \pi/4$ and $\eta = 0$ (○), $\eta = \pi/4$ (△), $\eta = 49\pi/100$ (∇), $\eta = 51\pi/100$ (◁), $\eta = 3\pi/4$ (▷), $\eta = \pi$ (⋄).

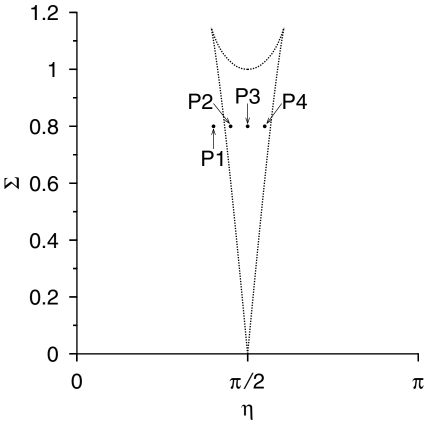

FIG. 6. The dotted line in the Σ-η plane separates the region within which there are four real solutions for ϕ_s, and the region outside where there are two real solutions for ϕ_s for a thin rod with shape factor $B = 1$.

side of Eq. (3) is zero, and the angle ϕ_s is determined by setting the right side of Eq. (4) equal to zero,

$$0 = -\frac{1}{2} - \frac{\cos(\phi_s)^2 - \sin(\phi_s)^2}{2} - \Sigma \sin(\phi_s - \eta). \tag{30}$$

The above equation can be reduced to a quartic equation for $\cos(\phi_s)$ using routine mathematical simplification,

$$\cos(\phi_s)^4 - 2\Sigma \sin(\eta)\cos(\phi_s)^3 + \Sigma^2 \cos(\phi_s)^2 - \Sigma^2 \cos(\eta)^2 = 0. \tag{31}$$

The discriminant Δ of the above quartic equation is

$$\Delta = -16\Sigma^6 \cos(\eta)^4\{\Sigma^4 + \Sigma^2[27\cos(\eta)^4 - 18\cos(\eta)^2 - 1] + 16\cos(\eta)^2\}. \tag{32}$$

The Eq. (31) has four distinct real roots for $\cos(\phi_s)$ for $\Delta < 0$, or

$$\begin{aligned} &\tfrac{1}{2}\{1 + 18\cos(\eta)^2 - 27\cos(\eta)^4 - \sqrt{[1-\cos(\eta)^2][1-9\cos(\eta)^2]^3}\} \\ &\quad \leqslant \Sigma^2 \leqslant \tfrac{1}{2}\{1 + 18\cos(\eta)^2 - 27\cos(\eta)^4 + \sqrt{[1-\cos(\eta)^2][1-9\cos(\eta)^2]^3}\}, \end{aligned} \tag{33}$$

and it has two distinct real roots otherwise. Clearly there are four distinct roots only for $-\frac{1}{3} < \cos(\eta) < \frac{1}{3}$, where the upper and lower limits in Eq. (33) are real. The domain for the existence of four distinct roots is the region within the dotted lines in Fig. 6 in the η-Σ plane, and there are two distinct roots outside of this region.

In Fig. 7 the phase plots and sample trajectories in the θ-ϕ parameter space are shown for four different locations, P1–P4, in Fig. 6. The phase portraits in Fig. 7 are mirror images about the vertical $\theta = \pi/2$ line, and therefore the phase portraits are shown in the left half and sample trajectories in the right half. Figure 7(a) shows that there is one stable node and one unstable node at point P1, which is outside of the dotted line in Fig. 6. In this case, all phase trajectories converge to the stable node. A second stable node and a saddle node appear in Fig. 7(b); this is consistent with the prediction from Fig. 6 that there are four roots at location P2. In Fig. 7(b) there are two distinct basins of attraction for the two stable nodes, separated by a separatrix that passes through the saddle node.

At the location P3 where $\eta = \pi/2$, the steady solutions of Eq. (30) are the roots of $\cos(\phi_s) = 0$, i.e., $\phi_s = \pm\pi/2$, and the locus $\cos(\phi_s) = \Sigma/\sin(\theta)$, as shown in Fig. 7(c). From Eq. (9), it can be inferred that the fixed point at $\phi_s = \pi/2$ is stable, and that at $\phi_s = -\pi/2$ is unstable. The

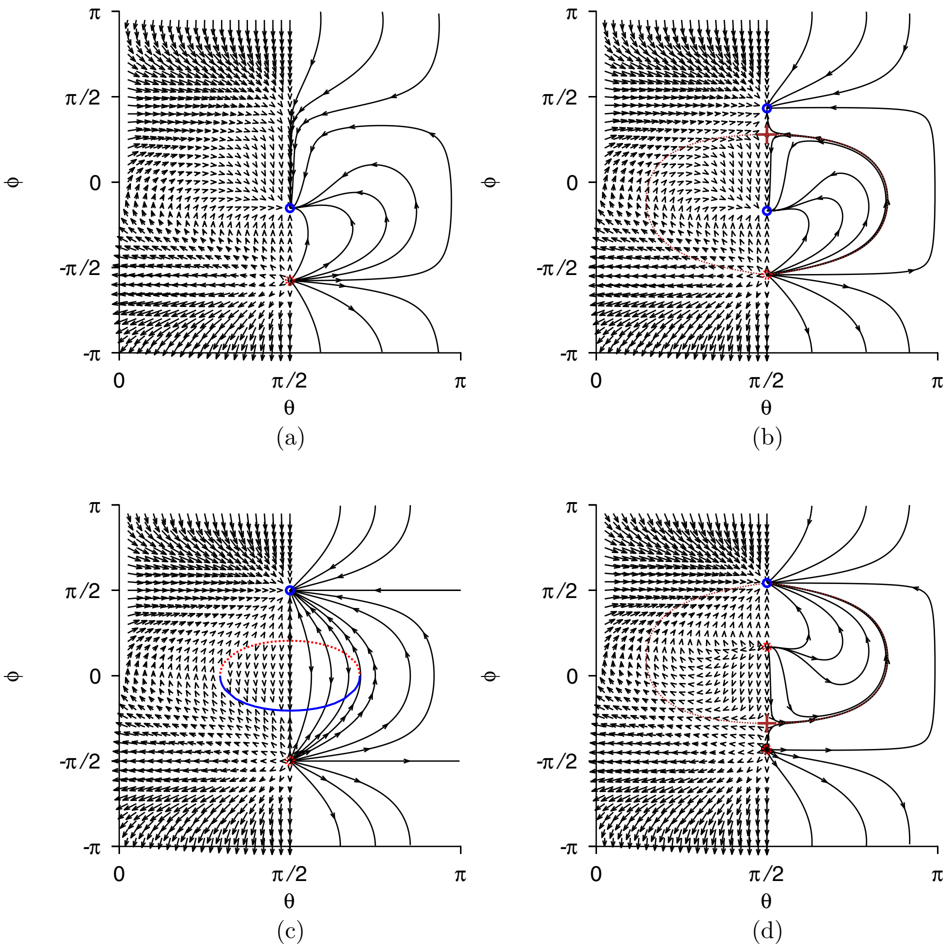

(a) (b) (c) (d)

FIG. 7. The phase portrait (left half) and sample trajectories (right half) in the θ-ϕ plane for a thin rod ($B = 1$) with $\Sigma = 0.8$, external field orientation $\xi = \pi/2$, and $\eta = 2\pi/5$ (point P1 in Fig. 6), $\eta = 9\pi/20$ (point P2 in Fig. 6), $\eta = \pi/2$ (point P3 in Fig. 6), and $\eta = 11\pi/20$ (point P4 in Fig. 6). The solid blue circles are stable nodes, the dashed red circles are unstable nodes, the brown plus is a saddle node and the brown dashed lines are separatrices between different basins of attraction/repulsion, the dashed red line is an unstable manifold, and the solid blue line is a stable manifold.

eigenvalues on the manifolds at $\cos(\phi_s) = [\Sigma/\sin(\theta_s)]$ are $(0, \Sigma^2\tan(\phi_s))$, and therefore the manifold for $\phi_s > 0$ is unstable, while that for $\phi_s < 0$ is stable. However, it should be noted that the solution for $B = 1$ is singular, because the right sides of Eqs. (3) and (4) are coincidentally equal to zero for $B = 1$ and $\cos(\phi_s) = [\Sigma/\sin(\theta_s)]$. When B is not exactly equal to 1, there are steady solutions in the flow plane at $\theta_s = \pi/2$ and $\cos(\phi_s) = \{[\Sigma \pm \sqrt{\Sigma^2 - 2B(1-B)}]/2B\}$; the latter exist only for $\Sigma^2 > 2B(1-B)$. For $(1-B) \ll 1$, the solutions for $\cos(\phi_s)$ are 0 and Σ. The manifolds $\cos(\phi_s) = [\Sigma/\sin(\theta_s)]$ are not solutions in the limit $(1-B) \ll 1$.

Figure 7(d) shows the phase portrait at the location P4 in Fig. 6. This phase portrait is related to that in Fig. 7(b) by the symmetry relation 4 in Sec. II A—the value of ϕ_s for the fixed points at P4 are the negative of those at P2, and the stability of the fixed points at P4 are the inverse of those at P2. Thus, it is sufficient to consider the phase portraits for $\eta \leqslant \pi/2$.

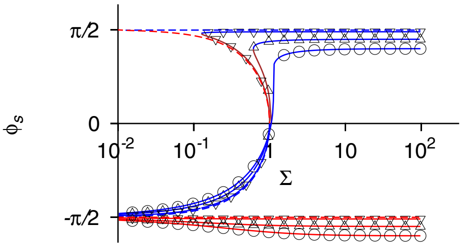

FIG. 8. The bifurcation diagram showing the trajectories of the stable (blue), unstable (red) and saddle (brown) nodes in the θ-ϕ plane as a function of the parameter Σ, for $\circ\ \eta = (2\pi/5)$, $\triangle\ \eta = (9\pi/20)$, $\nabla\ \eta = (49\pi/100)$, and dashed line $\eta = \pi/2$.

The angle ϕ_s for the fixed points is shown as a function of Σ in Fig. 8 for $\eta \leqslant \pi/2$. For $\Sigma > 1$, there is one stable and one unstable fixed point. The location of the unstable fixed point does not change significantly as Σ decreases. At $\Sigma = 1$, there is an inverse saddle-node bifurcation with the emergence of one stable and one saddle node at $\phi_s = 0$; the phase portrait containing two stable, one saddle, and one unstable node is shown in Fig. 7(b). These nodes move apart as Σ is decreased, until there is a second bifurcation in which the saddle node merges with one of the stable nodes, resulting in one stable and one unstable node, as shown in Fig. 7(a). The value of Σ at the saddle-node bifurcation decreases as the angle η increases, and in the limit $\eta \to \pi/2$, the value of Σ at the saddle-node bifurcation decreases to zero. For $\eta = \pi/2$, there is a ring of stationary points in the θ_s-ϕ_s plane, as shown in Fig. 7(b). However, this is a singular limit, as discussed above. For thin rods with $(1 - B) \ll 1$, there are two fixed points at $\theta_s = \pi/2$ and $\phi_s = \pm\pi/2$.

IV. PROLATE SPHEROID

A. Streamwise external field

The components $\hat{H}_X = 1, \hat{H}_Y = 0$, and $\hat{H}_Z = 0$, that is, $\xi = (\pi/2)$ and $\eta = (\pi/2)$, are substituted in Eqs. (3) and (4) when a streamwise external field is applied.

(1) One possible set of steady solutions for Eqs. (3) and (4) is obtained by setting $\cos(\theta_s) = 0$, so that Eq. (3) is trivially satisfied. The solution for ϕ_s is

$$\cos(\phi_s) = \frac{\Sigma}{2B} \pm \frac{1}{2}\sqrt{\left(\frac{\Sigma}{B}\right)^2 + 2\left(1 - \frac{1}{B}\right)}. \tag{34}$$

It should be noted that for each valid solution for $\cos(\phi_s)$, there are two possible solutions for ϕ_s which are of opposite sign.

The necessary condition for the existence of solutions for Eq. (34) is that the second term on the right side of Eq. (34) is real, that is,

$$\Sigma > \sqrt{2B(1 - B)}. \tag{35}$$

When the above condition is satisfied, there are two solutions for $\cos(\phi_s)$ (or four solutions for ϕ_s) which satisfy the condition condition $\cos(\phi_s) \leqslant 1$ for

$$\Sigma < \frac{(1 + B)}{2}. \tag{36}$$

When condition (36) is not satisfied, there is only one solution for $\cos(\phi_s)$ (or two solutions for ϕ_s) corresponding to the choice of the negative sign as the prefactor for the second term on the right in Eq. (34).

The eigenvalues of the linear stability matrix $\mathbf{L}$ [Eq. (9)] for the above solutions are

$$\lambda_\theta = \left[-\frac{\Sigma}{2} \pm \frac{\sqrt{\Sigma^2 - 2B(1-B)}}{2} \right] \sin{(\phi_s)}, \tag{37}$$

$$\lambda_\phi = \pm\sqrt{\Sigma^2 - 2B(1-B)} \sin{(\phi_s)}. \tag{38}$$

In Eqs. (37) and (38), the positive/negative sign on the right side is applicable when the positive/negative sign is used in the solution (34). When condition (36) is not satisfied and there are two solutions for ϕ_s obtained using the negative sign on the right side of Eq. (34), both eigenvalues in Eq. (37) are negative for $\phi_s > 0$ (stable fixed point) and both eigenvalues are positive for $\phi_s < 0$ (unstable fixed point). When condition (36) is satisfied, the two solutions obtained using the positive sign on the right side of Eq. (34) are both saddle points.

From Eqs. (35) and (36), it can be inferred that there is the possibility of four solutions for ϕ_s only for $\sqrt{2B(1-B)} < (1+B)/2$, or

$$B > \tfrac{1}{3}. \tag{39}$$

(2) The other possible solution of Eqs. (3) and (4) with $\xi = \pi/2$ and $\eta = \pi/2$ is obtained by setting $\sin{(\phi_s)} = 0$, so that Eq. (3) is identically satisfied. The angle θ_s is then obtained from Eq. (4),

$$\sin{(\theta_s)} = \frac{2\Sigma}{1+B}. \tag{40}$$

Clearly, the condition $\sin{(\theta_s)} < 1$ for the existence of solutions of Eq. (40) is identical to the condition for existence of four solutions for ϕ_s in Eq. (36). The eigenvalues of the linear stability matrix $\mathbf{L}$ [Eq. (8)] are imaginary,

$$\lambda_I = \pm\imath\sqrt{\frac{(1-B)((1+B)^2 - 4\Sigma^2)}{4(1+B)}}. \tag{41}$$

Thus, the stationary points are center nodes in the θ-ϕ plane. The ratio of the frequency of the orbits at the center nodes and the Jeffrey frequency, Eq. (11), is

$$\frac{\omega}{\omega_J} = \frac{\sqrt{(1+B)^2 - 4\Sigma^2}}{1+B}. \tag{42}$$

In summary, there are two bifurcations separating three distinct domains for a prolate spheroid with shape factor $B > \frac{1}{3}$ in a streamwise external field. For $\Sigma > (1+B)/2$, there are two stationary solutions for (θ_s, ϕ_s); these solutions are continuations of the solutions (13) and (14) for a high external field. For $\sqrt{2B(1-B)} < \Sigma < (1+B)/2$, there are six fixed points, four with $\theta_s = \pi/2$ where the spheroid is oriented in the X-Y plane, and two center nodes with $\sin{(\theta_s)} = [2\Sigma/(1+B)]$ where the orientation is not in the X-Y plane. For $\Sigma < \sqrt{2B(1-B)}$, there are no fixed points with orientation in the X-Y plane, and two center nodes having orientation in the X-Z plane $\sin{(\theta_s)} = [2\Sigma/(1+B)]$.

The phase portraits are shown in Fig. 9 for a prolate spheroid with $B = 0.6$. For $\Sigma < \sqrt{2B(1-B)}$, there are two center nodes at the locations specified with $\sin{(\phi_s)} = 0$ and $\sin{(\theta_s)}$ given by Eq. (40), as shown in Fig. 9(a). The phase plot consists of periodic orbits around these center nodes, and the frequency at the center nodes is predicted by Eq. (42). At $\Sigma = \sqrt{2B(1-B)}$, Fig. 9(b) shows the appearance of two saddle-node bifurcations simultaneously at the locations $\theta_s = \pi/2$, $\cos{(\phi_s)} = \sqrt{(1-B)/2B}$ and $\sin{(\phi_s)} = \pm\sqrt{(3B-1)/2B}$, in addition to the center node. As Σ is increased, there are two saddle nodes, one stable and one unstable node and two center nodes, as shown in Fig. 9(c). At $\Sigma = (1+B)/2$, the two saddle nodes and the two center nodes merge, resulting in one unstable and one stable node for $\Sigma > (1+B)/2$. The trajectory of the stationary points is shown in the bifurcation diagram in Fig. 10. For low Σ, the trajectory of two center nodes off the flow plane ($\theta_s \neq \pi/2$) is shown by the black dashed line. At $\Sigma = \sqrt{2B(1-B)}$

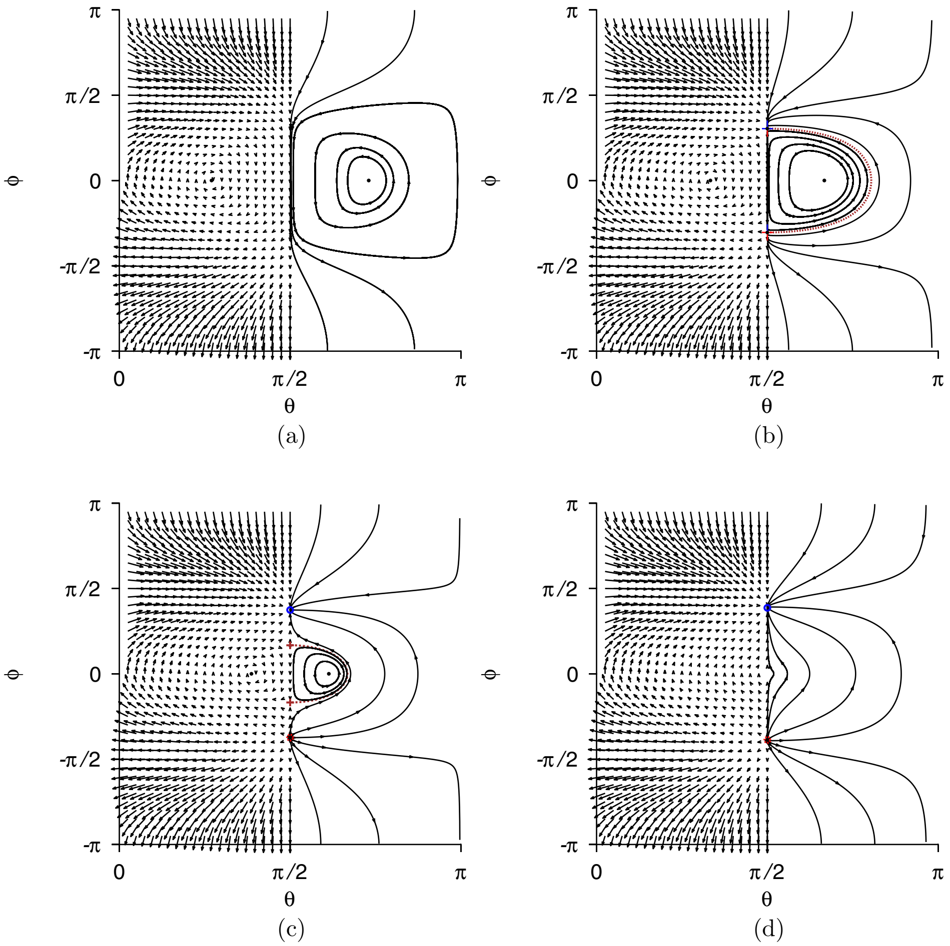

FIG. 9. The phase portrait in the θ-ϕ plane for a prolate spheroid when the external field is in the $+X$ direction ($\eta = \pi/2$), $B = 0.6$, $M = 0.6$ (a), $M = \sqrt{0.48}$ (b) $M = 0.75$ (c), and $M = 0.8$ (d). The blue solid circles are stable nodes, red dashed circles are unstable nodes, and the black solid circles are center nodes.

there are two symmetric saddle-node bifurcation points at B1, from which emerge one saddle node and one stable/unstable node each. As Σ is further increased, the saddle nodes and the two center nodes merge in a subcritical bifurcation at B2, resulting in one stable and one unstable node.

B. Cross-stream external field

For a cross-stream external field, the components $\hat{H}_X = 0$, $\hat{H}_Y = 1$, and $\hat{H}_Z = 0$, ($\xi = (\pi/2)$ and $\eta = \pi$), are substituted in Eqs. (3) and (4).

(1) One possible set of steady solutions for Eqs. (3) and (4) is obtained by setting $\cos(\theta_s) = 0$ so that Eq. (3) is trivially satisfied. The solution for $\sin(\phi_s)$ is

$$\sin(\phi_s) = -\frac{\Sigma}{2B} + \frac{1}{2}\sqrt{\left(\frac{\Sigma}{B}\right)^2 + 2\left(1 + \frac{1}{B}\right)}. \tag{43}$$

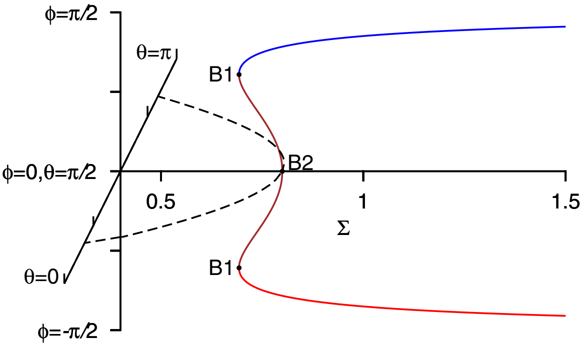

FIG. 10. The bifurcation diagram showing the trajectories of the center (black), stable (blue), unstable (red), and saddle (brown) nodes in the θ-ϕ plane as a function of the parameter Σ. The solid lines are on the $\theta = (\pi/2)$ plane, and the dashed line is perpendicular to the $\theta = (\pi/2)$ plane.

The magnitude of the solution is less than 1 only for

$$\Sigma > \frac{1-B}{2}. \tag{44}$$

Equation (43) provides two solutions for ϕ_s, one each for $0 \leqslant \phi_s \leqslant \pi/2$ and $\pi/2 \leqslant \phi_s \leqslant \pi$. The eigenvalues of the linear stability matrix $\mathbf{L}$ for these solutions are

$$\lambda_\theta = \left[\frac{\Sigma}{2} + \frac{\sqrt{\Sigma^2 + 2B(1+B)}}{2}\right]\cos(\phi_s), \tag{45}$$

$$\lambda_\phi = \sqrt{\Sigma^2 + 2B(1+B)}\cos(\phi_s). \tag{46}$$

Therefore, the solution with $0 \leqslant \phi_s \leqslant \pi/2$ is an unstable fixed point, and that with $\pi/2 \leqslant \phi_s \leqslant \pi$ is a stable fixed point.

(2) The other possible set of steady solutions is $\cos(\phi_s) = 0$ and

$$\sin(\theta_s) = \frac{2\Sigma}{1-B}. \tag{47}$$

The eigenvalues of the linear stability matrix $\mathbf{L}$ [Eq. (8)] are imaginary,

$$\lambda = \pm\imath \frac{\sqrt{(1+B)[(1-B)^2 - 4\Sigma^2]}}{2\sqrt{1-B}}. \tag{48}$$

The ratio of the frequency of frequency at the center nodes and the frequency of the Jeffrey orbits ω_J [Eq. (11)] is

$$\frac{\omega}{\omega_J} = \frac{\sqrt{[(1-B)^2 - 4\Sigma^2]}}{1-B}. \tag{49}$$

Thus, for a cross-stream external field, there are mutually exclusive parameter regimes for the existence of center nodes off the X-Y plane $[\Sigma < (1-B)/2]$ and a pair of attractive and repulsive stationary nodes on the X-Y plane $[\Sigma > (1-B)/2]$. The transition between these two takes place by the exchange of stability mechanism shown in Fig. 2 for a spherical particle.

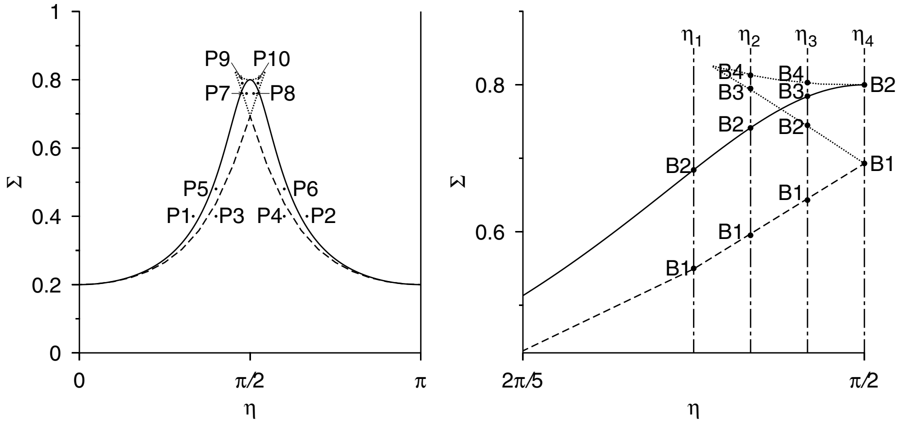

(a) (b)

FIG. 11. The lines in the Σ-η plane separating phase portraits of different topology (a) and a magnified view of the bifurcations that take place at different values of Σ (b) for a prolate spheroid with $B = 0.6$ in the presence of a external field.

C. Magnetic field in X-Y plane

In Fig. 11 the domains in the Σ-η plane which admit different types of solutions are shown for a prolate spheroid with $B = 0.6$. The region below the solid line in Fig. 11 satisfies the condition

$$\Sigma < \frac{1 - B^2}{2\sqrt{1 + B^2 + 2B\cos(2\eta)}}. \tag{50}$$

In this region, there are fixed points (θ_s, ϕ_s) for the director orientation [stationary solutions of Eqs. (3) and (4)] located off the X-Y plane, that is, $\theta_s \neq \pi/2$. Condition (50) is a generalization of the condition (36) for the streamwise external field ($\eta = \pi/2$) and the opposite of condition (44) for a cross-stream external field ($\eta = \pi$). Analytical solutions can be obtained for the angles θ_s and ϕ_s,

$$\tan(\phi_s) = \frac{-(1 + B)}{(1 - B)\tan(\eta)}, \tag{51}$$

$$\sin(\theta_s) = \frac{2\Sigma\sqrt{1 + B^2 + 2B\cos(2\eta)}}{1 - B^2}. \tag{52}$$

The above solution is a generalization of Eq. (40) for a streamwise external field ($\eta = \pi/2$) and Eq. (47) for a cross-stream external field ($\eta = \pi$). It is evident that the solution [Eq. (52)] is possible only if $\sin(\theta_s) \leqslant 1$ or if condition (50) is satisfied.

In the region above the dashed line but outside of the dotted line in Fig. 11, there are two solutions with orientation in the X-Y plane with $\theta_s = \pi/2$. In the region within the dotted line in Fig. 11, there are four solutions with orientation in the X-Y plane with $\theta_s = \pi/2$. The phase plots at specific locations, P1–P10, in these regions are discussed in further detail.

(1) At the locations P1 and P2 above the solid line, there are only two solutions with orientation along the X-Y plane, one of which is a stable node and the other an unstable node. These solutions are continuations of the asymptotic solutions (13) and (14) for high Σ, and the phase plots are qualitatively similar to those in Fig. 2(c).

(2) At the locations P3 and P4 below the dashed line, there are two solutions off the X-Y plane with $\theta_s \neq 0$. In contrast to the situation for a streamwise external field [Fig. 9(a)], these stationary points are not center nodes but are either stable or unstable depending on the value of η, as shown in Fig. 12. There is a stable/unstable limit cycle in the flow plane ($\theta = \pi/2$).

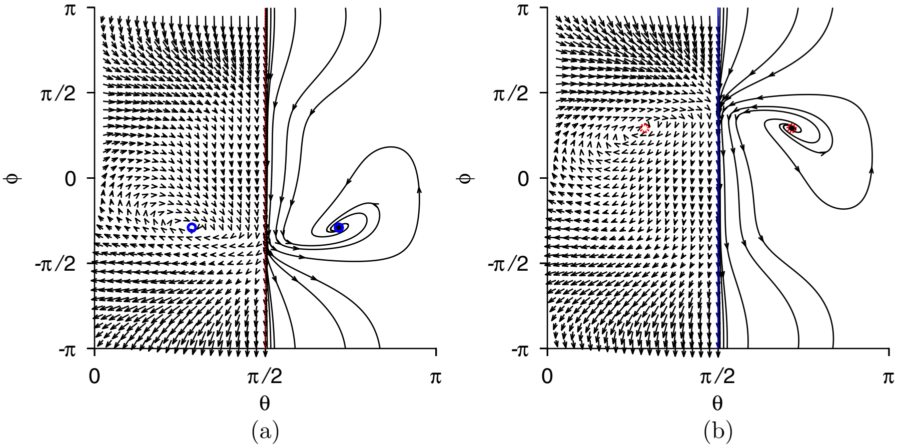

FIG. 12. The phase portrait in the θ-ϕ plane for a prolate spheroid with $B = 0.6$, $M = 0.4$, and $\eta = (2\pi/5)$ (a) and $(3\pi/5)$ (b) at the points P3 and P4, respectively, in Fig. 11. The solid blue circles are stable nodes, the dashed red circles are unstable nodes, the dashed red line is an unstable manifold, and the solid blue line is a stable manifold.

(3) At the points P5 and P6 in Fig. 11, there appear a saddle and a stable/unstable node along the flow plane at $\theta = \pi/2$, and the limit cycle on the flow plane ceases to exist, as shown in Fig. 13. There are two symmetric stable nodes off the flow plane for $\eta < \pi/2$, and two symmetric unstable nodes off the flow plane for $\eta > \pi/2$.

(4) There is a second bifurcation at the points P7 and P8, where other stable/unstable and saddle nodes appear, as shown in Fig. 14. This results in four stationary points along the flow plane and two stationary points off the flow plane, as shown in Fig. 14. For $\eta < \pi/2$, there simultaneously exist three stable nodes, two off the flow plane and one on the flow plane. Each has its individual basin of attraction, and the boundaries of the basins of attraction terminate at the saddle nodes.

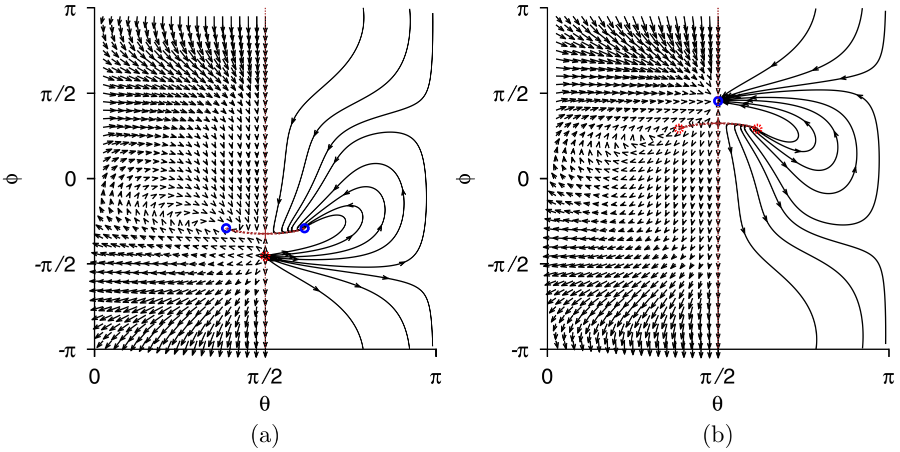

FIG. 13. The phase portrait in the θ-ϕ plane for a prolate spheroid with $B = 0.6$, $M = 0.48$, and $\eta = (2\pi/5)$ (a) and $(3\pi/5)$ (b) at the points P5 and P6, respectively, in Fig. 11. The solid blue circles are stable nodes, the dashed red circles are unstable nodes, the brown pluses are saddle nodes, and the brown dashed lines are separatrices between different basins of attraction/repulsion.

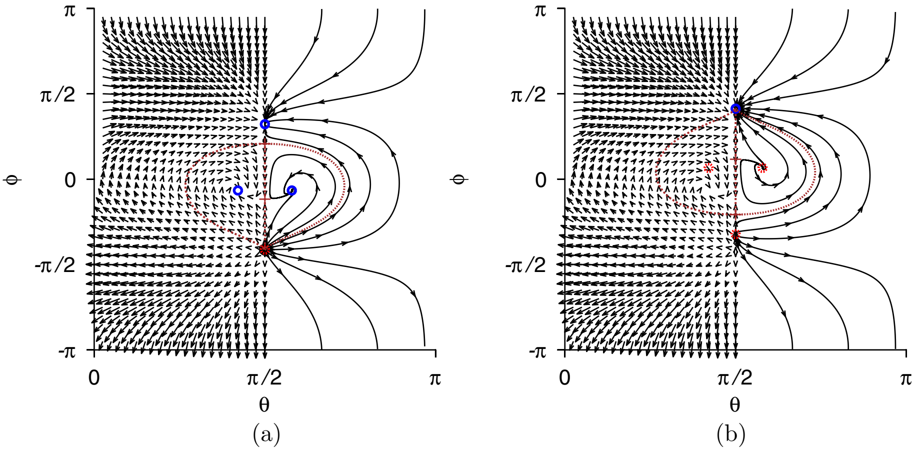

FIG. 14. The phase portrait in the θ-ϕ plane for a prolate spheroid with $B = 0.6$, $M = 0.76$, and $\eta = (29\pi/60)$ (a) and $(31\pi/60)$ (b) at the points P7 and P8, respectively, in Fig. 11. The solid blue circles are stable nodes, the dashed red circles are unstable nodes, the brown pluses are saddle nodes, and the brown dashed lines are separatrices between different basins of attraction/repulsion.

(5) At the locations P9 and P10 in Fig. 11, the two stable/unstable nodes off the flow plane merge with one of the saddle nodes, resulting in four stationary nodes on the flow plane, as shown in Fig. 15. For $\eta < \pi/2$, there are two stable, one unstable and one saddle node, and each stable node has its basin of attraction.

The different types of phase portraits arise from the bifurcations in the Σ-θ-ϕ space shown in Fig. 16 along vertical lines at different values of η in Fig. 11(b).

(1) Along the line $\eta = \eta_1$ in Fig. 11(b), Fig. 16(a) shows that there are two stable nodes when Σ is less than the value at B1 and an unstable stationary orbit along the flow plane. The phase portrait is as shown in Fig. 12(a). There is first one saddle-node bifurcation at the point B1 resulting in one

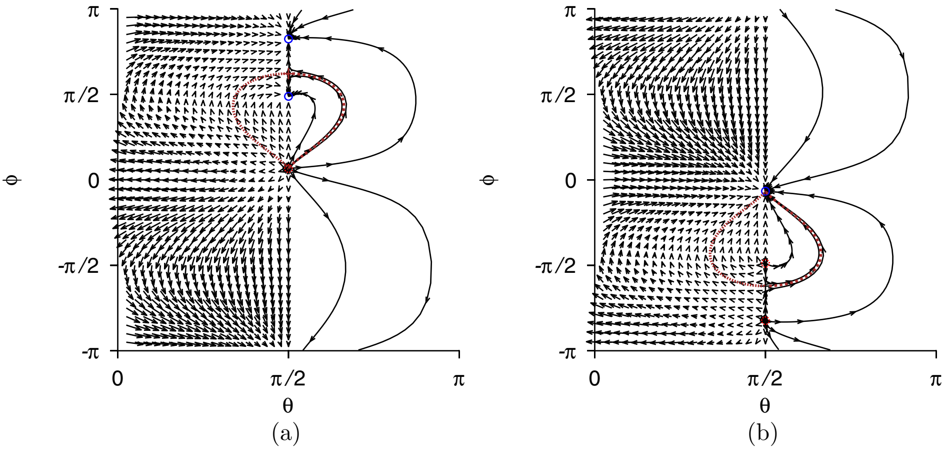

FIG. 15. The phase portrait in the θ-ϕ plane for a prolate spheroid with $B = 0.6$, $M = 0.8$, and $\eta = (19\pi/40)$ (a) and $(21\pi/40)$ (b) at the points P9 and P10, respectively, in Fig. 11. The solid blue circles are stable nodes, the dashed red circles are unstable nodes, the brown pluses are saddle nodes, and the brown dashed lines are separatrices between different basins of attraction/repulsion.

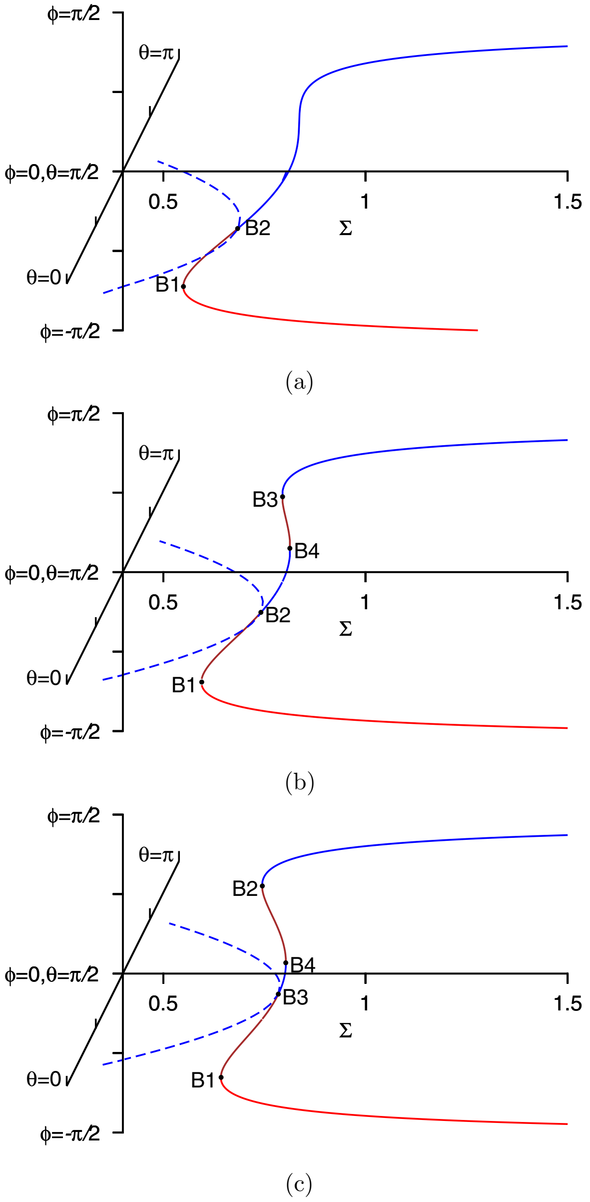

FIG. 16. The trajectories of the stationary points in the θ-ϕ-Σ space for $B = 0.6$, (a) along the vertical dash-dot line at $\eta_1 = 9\pi/20$ in Fig. 11(a), (b) along the vertical dash-dot line at $\eta_2 = 7\pi/15$ in Fig. 11(a), and (c) along the vertical dash-dot line at $\eta_3 = 29\pi/60$ in Fig. 11(a). The trajectories of the stable nodes are shown in blue, unstable nodes in red, and saddle nodes in brown. The trajectories shown by the solid lines are in the flow plane ($\theta = \pi/2$), and the trajectories shown by the dashed lines are off the flow plane. The unstable limit cycle in the flow plane when Σ is less than the value at B1 is not shown for simplicity.

unstable and one saddle node on the flow plane, in addition to the stable nodes off the flow plane. The phase portrait is as shown in Fig. 13(a). The saddle node which originates at B1 merges with the two stable fixed points on the flow plane at the bifurcation point B2, resulting in one stable and one unstable node when Σ is increased beyond the value at B2.

(2) Along the line $\eta = \eta_2$ in Fig. 11(b), there are two stable nodes off the flow plane when Σ is less than the value at B1, as shown in Fig. 16(c). There is one saddle-node bifurcation when the external field is increased to the value at B1 resulting in one unstable and one saddle node in the flow plane, in addition to the two stable nodes off the flow plane, as shown in Fig. 13(a). The saddle node and the two stable nodes off the flow plane merge at B2, resulting in one unstable and one stable node. There is a second saddle-node bifurcation at B3, resulting in one unstable, two stable and one saddle nodes on the flow plane, as shown in Fig. 14(a). When Σ is further increased, one stable and one unstable node merge at the subcritical bifurcation B4, resulting in one stable and one unstable node on the flow plane.

(3) Along the line $\eta = \eta_3$ in Fig. 11(b), there are two stable nodes when Σ is less than the value at B1, as shown in Fig. 16(c). There is one saddle-node bifurcation when the external field is increased to the value at B1 resulting in one unstable and one saddle node in the flow plane, in addition to the two stable nodes off the flow plane, as shown in Fig. 13(a). There is a second saddle-node bifurcation at B2, resulting in one unstable, one stable and two saddle nodes on the flow plane, in addition to two stable nodes off the flow plane, as shown in Fig. 14(a). When Σ is further increased, one unstable and one saddle node on the flow plane merge with the two stable nodes off the flow plane at B3, and phase portrait is of the type shown in Fig. 15(a), with two stable, one unstable, and one saddle node on the flow plane. One stable and one saddle node merge in a subcritical bifurcation B4, and there remain one stable and one unstable node.

Thus, a complicated sequence of phase portraits emerges from a simple sequence of two saddle-node bifurcations and two subcritical bifurcations, one of the latter involving the merger of two stable/unstable nodes off the flow plane, one stable/unstable node on the flow plane, and one saddle node. When the external field is in the flow direction, the bifurcation diagram shown in Fig. 10 is simpler, with two symmetric saddle-node bifurcations at the same value of Σ and one subcritical bifurcation. When the external field is in the velocity gradient direction, the saddle node and critical bifurcations occur simultaneously by the exchange of stability mechanism shown in Fig. 2.

The boundaries between different types of phase portraits are shown in Fig. 17 for different values of B. For a spherical particle with $B = 0$, there is only one bifurcation at $\Sigma = 0.5$, where two center nodes off the flow plane coalesce and one stable and one unstable node on the flow plane emerge, as shown in Fig. 2. For nonspherical particles, in the limit $\Sigma \ll 1$, there are two stable/unstable nodes off the flow plane and one unstable/stable limit cycle on the flow plane. The phase boundaries intersect the $\eta = 0$ axis at $\Sigma = (1 - B)/2$, and the $\eta = (\pi/2)$ axis at $\Sigma = (1 + B)/2$. For $\Sigma \gg 1$, there is one stable node where the particle is aligned along the external field, and one unstable node where the particle is aligned opposite to the external field. For $B < \frac{1}{3}$, there are only two bifurcations; there is a transition from the limit cycle to one stable/unstable and one saddle node on the flow plane on the dashed line. For $B > \frac{1}{3}$ there is the emergence of one more saddle and one unstable/stable node on the dotted line. At the solid line, the two nodes off the flow plane coalesce with one saddle node on the flow plane, and one stable/unstable node remains. As the value of B increases, the domain between the solid and dashed line shrinks, and the domain within the dotted line increases.

The thin rod, $B = 1$, is a singular limit where the region below the solid and dashed lines shrinks to zero. There are no stationary nodes off the flow plane, and there are two/four stationary nodes inside/outside the dotted domain in Fig. 6 on the flow plane even in the limit $\Sigma \to 0$. For $(1 - B) \ll 1$, the solid boundary (for stationary nodes off the flow plane) is given by Eq. (50), which tends to $(1 - B)/2$ for $\eta = 0$. This is the region above the solid boundary in Fig. 17 when η is not close to $\pi/2$. The dashed line, which is the boundary between no solutions and two solutions in the flow plane, intersects the $\eta = 0$ axis at $\Sigma = (1 - B)/2$, and it is proportional to $(1 - B)/[2|\cos(\eta)|]$ for $|\cos(\eta)| \gg \sqrt{1 - B}$. This is consistent with the condition for the existence of solutions (24) and (25). For $|\cos(\eta)| \ll \sqrt{1 - B}$, the dashed line approaches $\sqrt{2(1 - B)} - 2|\cos(\eta)|$; this is consistent with the conditions, obtained by substituting $\xi = \pi/2$ and $\theta_0 = \pi/2$, in Eqs. (28) and (29). Therefore, even when B is close to 1, there are significant regions in the Σ versus η plane involving stable/unstable nodes off the flow plane.

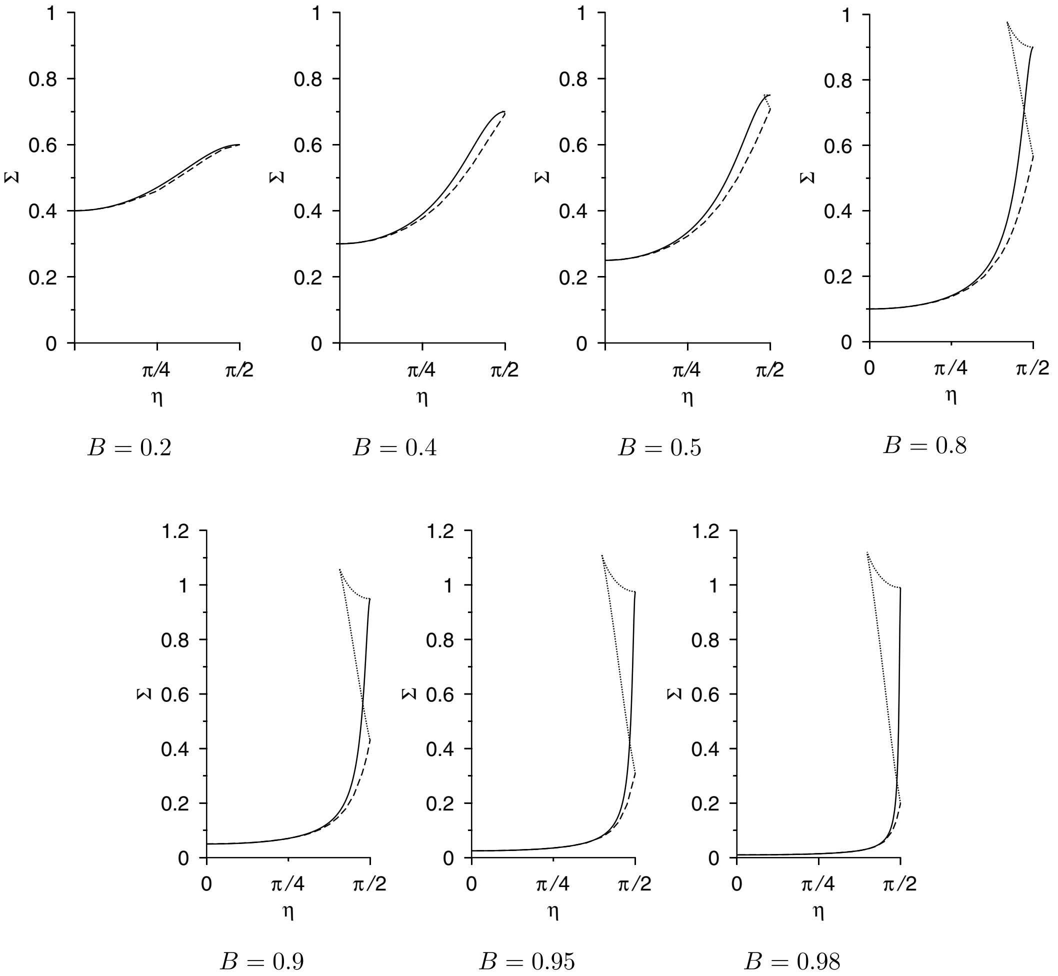

$B = 0.2$ $B = 0.4$ $B = 0.5$ $B = 0.8$

$B = 0.9$ $B = 0.95$ $B = 0.98$

FIG. 17. The lines in the Σ-η plane separating phase portraits of different topology.

V. CONCLUSIONS

The primary results of the present analysis are the sequence of bifurcations, shown in Fig. 16, along different vertical lines in Fig. 11(b), which result in the rich variety of the phase space topologies shown in Figs. 12 to 15 when the external field is along the flow plane. The different topologies are delineated by only three phase boundaries shown by the solid, dotted, and dashed lines in Fig. 11(a). The dashed line separates a regions with zero fixed points (below) and two fixed points (above) along the flow plane. The dotted line is the boundary between regions of two fixed points on the flow plane (outside the region) and four fixed points on the flow plane (within the region). These two were first reported in Ref. [22] for a spheroid with orientation restricted in the flow plane. The solid line separates the regions between two fixed points off the flow plane (below) and zero fixed points off the flow plane (above); this phase boundary is present only for a three-dimensional system. Different locations in the Σ-η parameter space have different types of phase behavior.

When the angle η of the external field is $(\pi/2)$, that is, the external field is in the flow direction, a series of bifurcations occurs as shown in Fig. 10. For small Σ, there are two center nodes off the flow plane, as shown in Fig. 9. As Σ is increased, there are two symmetric subcritical bifurcations when the external field crosses the value at B1 in Fig. 10. For Σ between B1 and B2, the phase portrait contains two center nodes off the flow plane, and two saddle nodes on the flow plane, as shown in Fig. 10. There is a saddle node at the location B2 in Fig. 10, after which the phase portrait contains one stable and one unstable node.

For an oblique external field with $\eta \neq 0, \pi/2$, there are two stable/unstable nodes off the flow plane for low Σ, as shown in Fig. 12. If the two stationary points are stable (unstable), the rotating trajectory in the flow plane ($\theta = \pi/2$) is unstable (stable). For a high external field, there is one stable and one unstable stationary point along the flow plane, $\theta = \pi/2$. The transition between these two phase portraits occurs in complex ways as the strength of the external field is increased, as shown in Figs. 13–15. All of these involve two saddle-node bifurcations, one subcritical bifurcation and one merger of the low Σ solutions off the flow plane with the solution branch on the flow plane, as shown in Fig. 16.

The other significant result of the present analysis is the singular nature of the thin rod limit $B = 1$. A comparison of Fig. 17 and Fig. 6 shows that there are only two domains for a thin rod, but there are at least four domains with a significantly more complicated phase portrait even for $B = 0.98$. Thus, the dynamics of a high aspect ratio spheroid could be very different from that for the ideal thin rod. The phase portrait in Fig. 7 for an ideal thin rod is also qualitatively different from that for a spheroid with high aspect ratio. The phase portrait in Fig. 7(c) has continuous stable/unstable lines for an ideal thin rod, but there are only two fixed points along the flow plane at $\theta = (\pi/2)$ for a high aspect ratio spheroid. Thus, there are several aspects of the dynamics of a thin rod which are qualitatively different from that for a prolate spheroid with high aspect ratio.

The dynamics of a thin rod, analyzed in Sec. III, also shows interesting behavior. The orientation of the rod is sensitively dependent on the cross-stream component $\hat{H}_Y$ for the external field. Equation (20) shows that the orientation changes discontinuously when $\hat{H}_Y$ passes through zero for $\Sigma \ll 1$. There is no such discontinuous change for $\Sigma \gg 1$, where the particle orientation is along the direction of the external field. This results in a near-discontinuous change in the particle orientation as the strength of the external field is increased, as shown in Fig. 4. This also results in a discontinuous change in the torque on the particle, as shown in Fig. 5. This transition in the particle orientation should be observable in experiments both for a thin rod and for a thin disk (due to the symmetry between a thin rod and thin disk discussed in Sec. II A).

ACKNOWLEDGMENT

The author would like to thank the Department of Science and Technology, the Government of India, and the J. R. D. Tata Memorial Trust for financial support.

[1] H. K. Moffat, On the behaviour of a suspension of conducting particles subjected to a time-periodic magnetic field, J. Fluid Mech. **218**, 509 (1990).

[2] R. Zhou, F. Bai, and C. Wang, Magnetic separation of microparticles by shape, Lab Chip **17**, 401 (2017).

[3] R. Zhou, C. A. Sobecki, J. Zhang, Y. Zhang, and C. Wang, Magnetic Control of Lateral Migration of Ellipsoidal Microparticles in Microscale Flows, Phys. Rev. Appl. **8**, 024019 (2017).

[4] D. Matsunaga, F. Meng, A. Zottl, R. Golestanian, and J. M. Yeomans, Focusing and Sorting of Ellipsoidal Magnetic Particles in Microchannels, Phys. Rev. Lett. **119**, 198002 (2017).

[5] D. Matsunaga, A. Zöttl, F. Meng, R. Golestanian, and J. M. Yeomans, Far-field theory for trajectories of magnetic ellipsoids in rectangular and circular channels, IMA J. Appl. Math. **83**, 767 (2018).

[6] R. S. Allan and S. G. Mason, Particle behavior in shear and electric fields. II. Rigid rods and spherical doublets, Proc. R. Soc. London Ser. A **267**, 62 (1962).

[7] A. Okagawa, R. G. Cox, and S. G. Mason, Particle behavior in shear and electric fields. VI. The microrheology of rigid spheroids, J. Colloid Interface Sci. **47**, 536 (1974).

[8] S. T. Demetriades, Effect of electrostatic fields on the orientation of colloidal particles immersed in shear flow, J. Chem. Phys. **29**, 1054 (1958).

[9] D. J. Klingenberg, Magnetorheology: Applications and challenges, AIChE J. **47**, 246 (2001).

[10] S. G. Sherman, A. C. Becnel, and N. M. Wereley, Relating Mason number to Bingham number in magnetorheological fluids, J. Magn. Magn. Mater. **380**, 98 (2015).

[11] A. V. Anupama, V. Kumaran, and B. Sahoo, Magnetorheological fluids containing rod-shaped lithium-zinc ferrite particles: The steady-state shear response, Soft Matter **14**, 5407 (2018).

[12] K. M. Jansons, Determination of the constitutive equations for a magnetic fluid, J. Fluid Mech. **137**, 187 (1983).

[13] M. T. Lopez-Lopez, P. Kuzhir, and G. Bossis, Magnetorheology of fiber suspensions. I. Experimental, J. Rheol. **53**, 115 (2009).

[14] P. Kuzhir, M. T. Lopez-Lopez, and G. Bossis, Magnetorheology of fiber suspensions. II. Theory, J. Rheol. **53**, 127 (2009).

[15] D. J. Klingenberg and C. F. Zukoski, Studies on the steady-shear behavior of electrorheological suspensions, Langmuir **6**, 15 (1990).

[16] D. Vagberg and B. P. Tighe, On the apparent yield stress in non-Brownian magnetorheological fluids, Soft Matter **13**, 7207 (2017).

[17] A. D. Shine and R. C. Armstrong, The rotation of a suspended axisymmetric ellipsoid in a magnetic field, Rheol. Acta **26**, 152 (1987).

[18] G. B. Jeffrey, The motion of ellipsoidal particles immersed in a viscous fluid, Proc. Roy. Soc. A **102**, 161 (1922).

[19] E. J. Hinch and L. G. Leal, Rotation of small non-axisymmetric particles in a simple shear flow, J. Fluid Mech. **92**, 591 (1979).

[20] I. Puyesky and I. Frankel, The motion of a dipolar spherical particle in homogeneous shear and time-periodic fields, J. Fluid Mech. **369**, 191 (1998).

[21] Y. Almog and I. Frankel, The motion of axisymmetric dipolar particles in a homogeneous shear flow, J. Fluid Mech. **289**, 243 (1995).

[22] C. A. Sobecki, J. Zhang, Y. Zhang, and C. Wang, Dynamics of paramagnetic and ferromagnetic ellipsoidal particles in shear flow under a uniform magnetic field, Phys. Rev. Fluids **3**, 084201 (2018).

[23] H. Goldstein, *Classical Mechanics* (Narosa Publishing House, New Delhi, 1989), chapter 4.